

Terahertz Channel Measurement and Analysis on a University Campus Street

Yiqin Wang¹, Yuanbo Li¹, Yi Chen², Ziming Yu², and Chong Han¹

¹Terahertz Wireless Communications (TWC) Laboratory, Shanghai Jiao Tong University, China.

Email: {wangyiqin, yuanbo.li, chong.han}@sjtu.edu.cn

²Huawei Technologies Co., Ltd., China. Email: {chenyi171, yuziming}@huawei.com

Abstract—Owning abundant bandwidth resource, the Terahertz (0.1-10 THz) band is a promising spectrum to support sixth-generation (6G) and beyond communications. As the foundation of channel study in the spectrum, channel measurement is ongoing in covering representative 6G communication scenarios and promising THz frequency bands. In this paper, a wideband channel measurement in an L-shaped university campus street is conducted at 306-321 GHz and 356-371 GHz. In particular, ten line-of-sight (LoS) and eight non-line-of-sight (NLoS) points are measured at the two frequency bands, respectively. In total, 6480 channel impulse responses (CIRs) are obtained from the measurement, based on which multi-path propagation in the L-shaped roadway in the THz band is elaborated to identify major scatterers of walls, vehicles, etc. in the environment and their impact on multi-path components (MPCs). Furthermore, outdoor THz channel characteristics in the two frequency bands are analyzed, including path losses, shadow fading, cluster parameters, delay spread and angular spread. In contrast with the counterparts in the similar outdoor scenario at lower frequencies, the results verify the sparsity of MPCs at THz frequencies and indicate smaller power spreads in both temporal and spatial domains in the THz band.

I. INTRODUCTION

As a promising spectrum band for sixth-generation (6G) communications, the Terahertz (0.1-10 THz) band is anticipated to meet the demand of wireless systems for data rates to reach terabits per second (Tbps) [1]–[3]. In this new spectrum, the design of wireless systems relies on the study of THz wireless channels, which includes physical measurement of channels, analysis of channel characteristics, among others [4]. Compared with well investigated centimeter-wave (cmWave) and millimeter-wave (mmWave) bands, the exploration of THz wireless channels, especially the physical measurement of THz wireless channels, is far from sufficient to cover all representative 6G communication scenarios and promising THz frequencies.

Channel measurement campaigns have been conducted mainly at 140 GHz, 190 GHz, and 220 GHz [4]–[6], i.e., in the “sub-THz” band that overlaps with the mmWave band [3]. By contrast, wireless channel measurements above 300 GHz are still inadequate. In the up-to-date acts of the World Radiocommunication Conference 2019 (WRC-19), the frequency bands from 275 GHz to 450 GHz have identified for the implementation of fixed and land mobile service applications [7]. Some existing measurement studies in these

frequency bands are conducted in indoor hallways [8], [9], an aircraft cabin [10], a courtyard [11], and railway and vehicular communication scenarios [12], [13].

Nevertheless, channel measurement campaigns above 300 GHz hardly go to outdoor scenarios. Besides, most of these studies use correlation-based channel sounder with measuring bandwidth no more than 8 GHz. To fill this research gap, the contributions of this work include that we present a wideband vector network analyzer (VNA)-based channel measurement campaign conducted in a typical outdoor scenario in two frequency bands above 300 GHz, with measuring bandwidth of 15 GHz. In specific, the measurement campaign is conducted in an L-shaped street on a university campus at 306-321 GHz and 356-371 GHz. The scenario features one street along the parking area, and the other perpendicular street canyon between two buildings. Both line-of-sight (LoS) and non-line-of-sight (NLoS) cases are investigated, with 18 measuring positions and 6480 channel impulse responses (CIRs) in total. In light of the measurement results, we retrieve the propagation of multi-path components (MPCs) in the L-shaped street. Major MPC contributors in the environment, namely walls, vehicles, traffic signs and lamp poles, are identified, and their impacts by means of transmission, reflection, and scattering of MPCs are explored. Channel characteristics in the two frequency bands are analyzed in depth, including the path losses, shadow fading, cluster parameters, delay spread and angular spreads. Furthermore, we compare our results with those in the Urban Micro (UMi)-street canyon scenario specified in 3rd Generation Partnership Project (3GPP) Technical Report (TR) 38.901 [14], which indicates the sparsity of MPCs and smaller power spreads in both temporal and spatial domains in the THz band.

The remainder of this paper is organized as follows. The wideband VNA-based channel sounder system and the measurement campaign are introduced in Sec. II. We then present channel measurement results in Sec. III. Specifically, major scatterers in the environment and their impact on MPCs are investigated, and channel characteristics are analyzed. Finally, the paper is concluded in Sec. IV.

II. CHANNEL MEASUREMENT CAMPAIGN

In this section, we introduce our VNA-based channel measurement platform, and describe the THz measurement

TABLE I: Parameters of the measurement.

Parameter	Value
Frequency band	306-321, 356-371 GHz
Bandwidth	15 GHz
Sweeping interval	2.5 MHz
Sweeping points	6001
Time resolution	66.7 ps
Space resolution	2 cm
Maximum excess delay	400 ns
Maximum path length	120 m
Tx antenna gain	7 dBi
Tx 3-dB beamwidth	60°
Rx antenna gain	25-26 dBi
Rx 3-dB beamwidth	8°
Tx height	3 m
Rx height	1.75 m
Rx azimuth angles	[0° : 10° : 360°]
Rx elevation angles	[-20° : 10° : 20°]
Average noise floor	-180 dBm
Dynamic range	119 dB

campaign at 306-321 GHz and 356-371 GHz in a L-shaped street on the campus of Shanghai Jiao Tong University (SJTU).

A. Channel Measurement System

Our channel measurement platform supports the frequency ranging from 260 GHz to 400 GHz. As detailed in [8], the system is composed of THz transmitter (Tx) and receiver (Rx) modules and the Ceyear 3672C VNA. The system calibration procedure is described in detail in our previous works [8], [9]. In this measurement campaign, we investigate two frequency bands, 306-321 GHz and 356-371 GHz, which both cover the bandwidth of 15 GHz. The frequency sweeping interval is 2.5 MHz, resulting in 6001 sweeping points for each pair of Tx-Rx directions. Therefore, the space resolution is 2 cm and the maximum detectable path length is 120 m. To compensate for the high path loss in the THz band, waveguides and WR2.8 horn antenna are installed, with gains around 7 dBi (3-dB beamwidth around 60°) at the Tx side and 25-26 dBi (3-dB beamwidth around 8°) at the Rx side, respectively.

Regarding the mechanical part of the measurement system, the Tx and Rx are lifted to reach the height of 3 m and 1.75 m, respectively. The Tx is static, while by contrast, to receive MPCs, the Rx is driven by the rotator to scan the complete azimuth domain and from -20° to 20° in the elevation domain, with the step of 10°. Key parameters of the measurement are summarized in Table I.

B. Measurement Deployment

As shown in Fig. 1, the measurement campaign is conducted in the outdoor street bounded by Wenbo Building, Longbin Building, and Nanyang Road on the SJTU campus. Specifically, we focus on the L-shaped turning at the cross-road, depicted as the yellow region, with buildings, vehicles,

pedestrians, plants, etc. The west street (Street A) is parallel to Nanyang Road, and is between the west wall of Wenbo Building and a parking area. Vehicles, lamp poles and traffic signs are found along Street A, and one lamp pole is at the southwest corner of Wenbo Building. The other street canyon (Street B) between two buildings is about 22.32 m wide. Plants and a non-automobile parking area are located in the south of Wenbo Building along Street B.

The measurement deployment is illustrated in Fig. 2. We set west when the horizontal angle φ equals to 0°, while the value of φ increases clockwise. Tx is located at the northwest corner in Street A, i.e., 29.66 m away from the junction of two streets. The directivity of Tx points to the southeast direction, with the fixed horizontal angle of $\varphi = 230^\circ$ and elevation angle of $\theta = 0^\circ$. The positions of Rx are distributed along two segments of the L-shaped street, labeled as Rx1-Rx8 and Rx9-Rx16. The farthest point is about 20 m away from the junction of two streets. Moreover, two additional Rx points, Rx17 and Rx18, are located in the non-automobile parking area, to simulate user equipment in the shadow of a building. To classify, Rx1 to Rx10 belong to the LoS case, while Rx11 to Rx18 belong to the NLoS case.

Interestingly, the source power of the sounder systems is supplied by a hybrid vehicle, which is parked in the parking area in Street A in the LoS case. By contrast, due to the limit of cable length, it is parked at the southwest corner of Wenbo Building when we measure channel responses at NLoS points, as shown in Fig. 1(b). Note that this vehicle creates transmission, reflection and scattering in the measurement.

III. CHANNEL ANALYSIS AND CHARACTERIZATION

In this section, power-delay-angle profile (PDAP) is analyzed for multi-path characterization in the L-shaped street. Moreover, channel features in two frequency bands are analyzed in depth, including path losses, shadow fading, cluster parameters, delay spread and angular spread.

A. Power-Delay-Angle-Profile (PDAP) Analysis

The PDAP results at 306-321 GHz are taken as examples, while the results in the two bands are summarized and compared in Table II. First, for Rx1 to Rx4, as shown in Fig. 3, three categories of MPCs are detected, namely, LoS, forward-reflected, and back-reflected rays from the wall. First, the LoS ray with azimuth angle of arrival (AoA, φ) equals to 60-70°, travels 34.27 ns, 40.53 ns, 49.87 ns, and 55.93 ns, to reach Rx1-4. These LoS time-of-arrival (ToAs) correspond to the path length of 10.28 m, 12.16 m, 14.96 m, and 16.78 m, respectively. The power value varies from -104 dB to -113 dB.

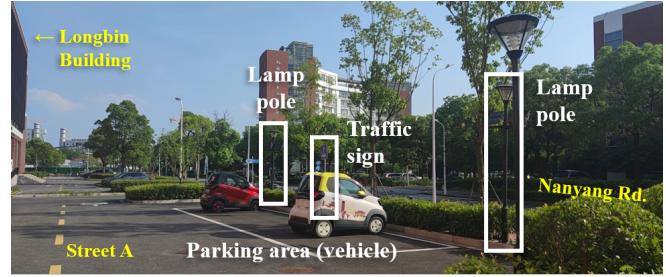
Second, the forward-reflected rays are attributed to the reflection on the west wall of Wenbo Building, with φ ranges over 120-130°. The traveling path length is around 3 m longer than the LoS ray. The extra loss of wall forward-reflection is measured about 5-15 dB. By contrast, the third type of rays back-reflect from the west wall of Wenbo Building, with φ ranges over 250-260°, and propagate over 30.6 m to 23.7 m. The power is around -140 dB, which denotes that the extra



(a) The top view of the measurement campaign.



(b) The photo of the environment.



(c) The photo of the west street (Street A).

Fig. 1: Measurement campaign in the L-shaped street on the SJTU campus.

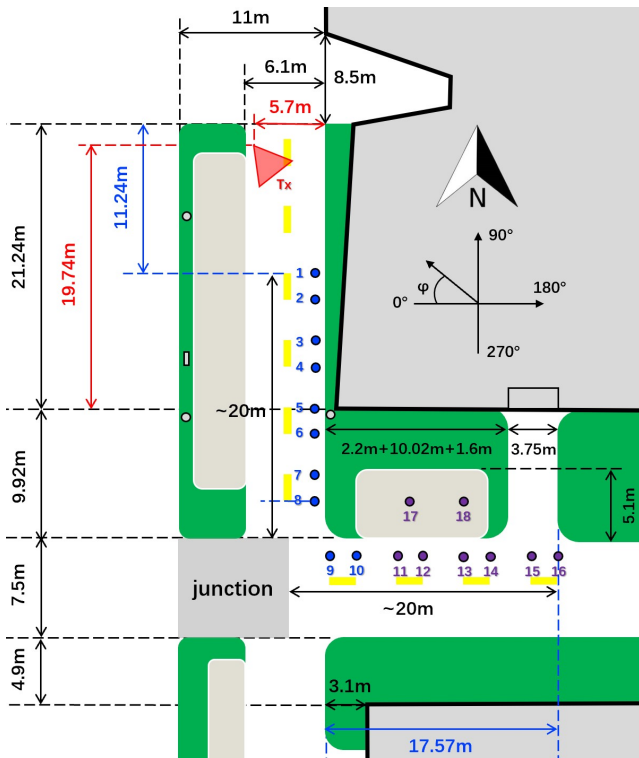


Fig. 2: Measurement deployment in the L-shaped street on the SJTU campus (Tx, red; LoS Rx, blue; NLoS Rx, violet).

loss of wall back-reflection is about 20-30 dB, i.e., noticeably higher than the forward-reflection. In our measurement, due to the geometry, the back-reflected rays from Wenbo Building can only be observed at Rx1-4.

Interestingly, between the two wall reflected rays, we observe a tail in PDAP with an increasing delay, a larger AoA and decreasing power, which demonstrates the continuous scattering from the wall. This phenomena occurs since the Tx and Rx positions are close to the wall of Wenbo Building. Therefore, the power of scattered rays from the wall material is above the noise floor. Moreover, as Rx1-4 are distributed in parallel with the wall, we can also observe continuous change of delays (and thus the values of power) and AoAs of scattering rays among PDAPs.

As shown in Fig. 4, besides the LoS ray and the forward-reflected ray from the wall, reflected rays from the lamp pole and the traffic sign are detected at Rx5 and Rx6. Reflected from the lamp pole at the southwest corner of Wenbo Building, the reflected ray is observed at Rx5 with φ equals to 200° . Moreover, coming from the traffic sign beside the parking lot, the reflected ray is observed at Rx6 with φ equals to 30° . To compare the reflection losses, the lamp pole reflection loss is about 15 dB, while the traffic sign, as a flat metal plane, results in much lower loss, e.g., around 6-8 dB.

Moving to the south direction further, Rx7-10 are the last four LoS positions, where the received MPCs are similar. Fig. 5 takes Rx8 and Rx10 as examples. First, the LoS ray and the back-reflected rays from Longbin Building can be observed. The back-reflection of the wall causes additional loss of 28-30 dB. Similar to other LoS Rx positions, sporadic rays

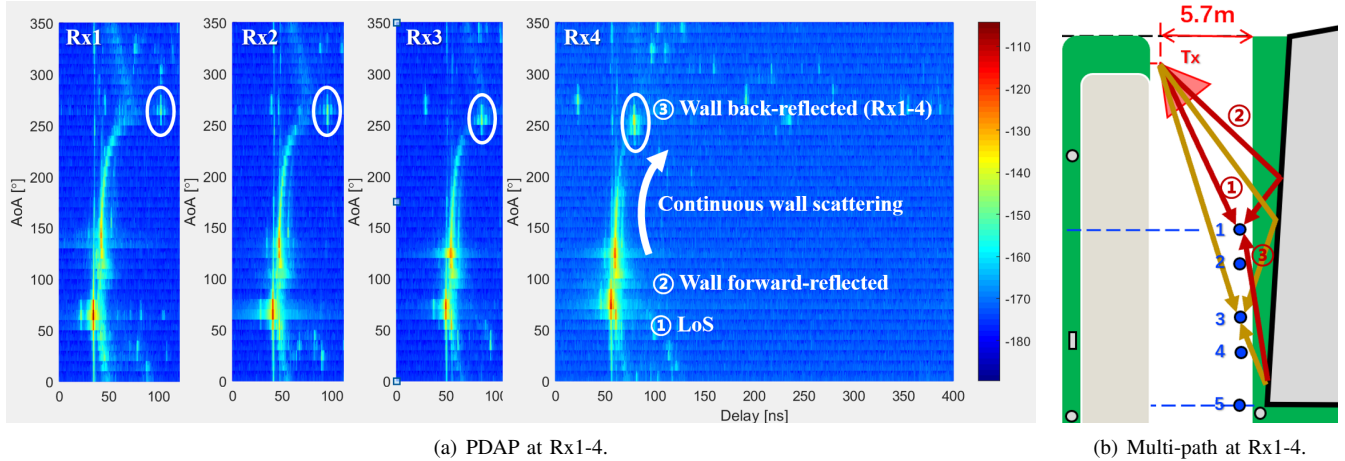


Fig. 3: PDAPs and multi-path propagation analysis at Rx1-4.

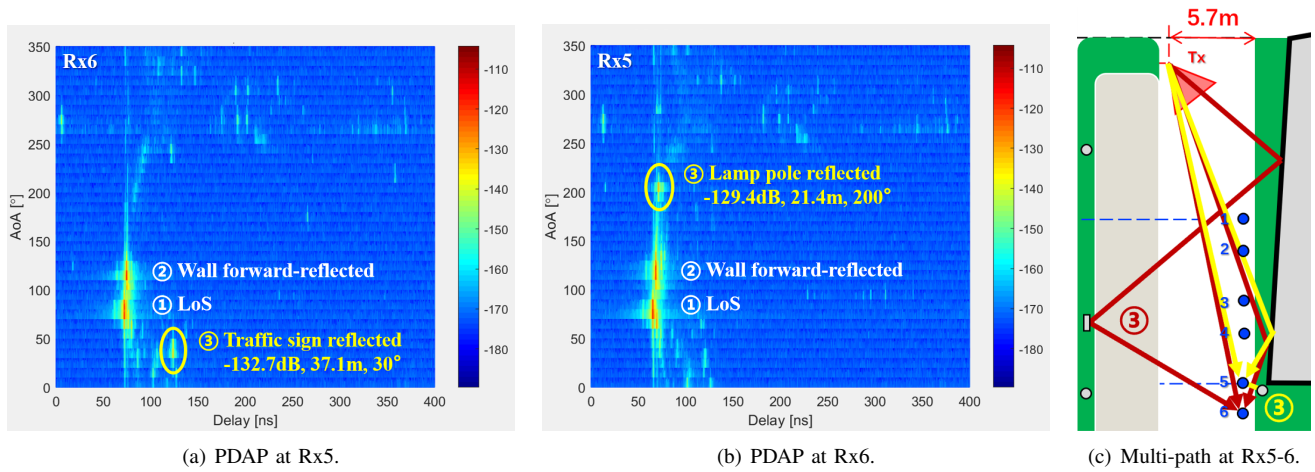


Fig. 4: PDAPs and multi-path propagation analysis at Rx5-6.

from the parking lot are detected, i.e., with φ in the range of $0\text{-}90^\circ$. The scatterers include vehicles, lamp poles ($30^\circ\text{-}40^\circ$), traffic signs ($50^\circ\text{-}60^\circ$), and plants. However, unlike strong reflected rays (e.g., with power around -130 dB) at Rx5 and Rx6, these scattering rays are much weaker, with power around -150 dB, i.e., additional 20 dB losses.

When the receiver moves to NLoS positions, as noted in Section II, a hybrid vehicle is parked at the southwest corner of Wenbo Building to outsource power for the channel sounder system. As summarized in Fig. 6, the rays mainly come from (i) the first-order forward-reflection from Longbin Building, (ii) the higher-order reflection between two buildings, (iii) the transmission through the vehicle, and (iv) the scattering from vehicles in the parking area and near Longbin Building. First, the highest received power is -130 dB in the NLoS case. Second, the reflection loss caused by the wall of Longbin Building varies from 18 dB to 30 dB, depending on the angle of incidence. Third, the transmission loss through the vehicle is less than 10 dB, deduced based on the comparison with the reflected ray from the traffic sign at Rx6. By contrast,

the power of the scattering rays from vehicles is as low as -150 dB at NLoS Rx points, which indicates less significance of scattering (compared to reflection) on vehicles.

B. Characteristic Analysis

Based on the data post-processing procedures as detailed in [15], we present the channel characteristics in depth. We clarify that we only focus on MPCs within the dynamic range of 30 dB, in order to be compatible with the lower dynamic range of general THz devices [4]. In Table II, statistical channel parameters in two frequency bands are summarized and compared with those in the UMi-street canyon scenario specified in 3GPP TR 38.901 [14], which are discussed as follows.

1) *Path loss and shadow fading*: The best direction path loss and the omni-directional path loss [8] are investigated. The close-in (CI) and α - β path loss models are invoked, which are expressed respectively as

$$PL^{CI} = 10 \times PLE \times \log_{10} \frac{d}{d_0} + FSPL(d_0) + X_{\sigma_{SF}}^{CI}, \quad (1a)$$

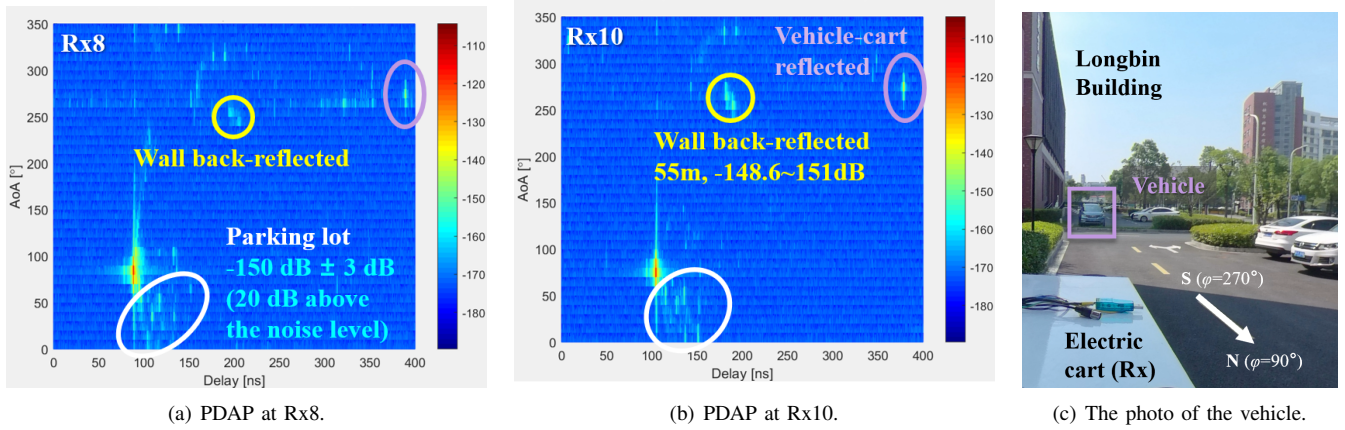


Fig. 5: PDAPs at Rx8, Rx10 and the vehicle reflection in the south.

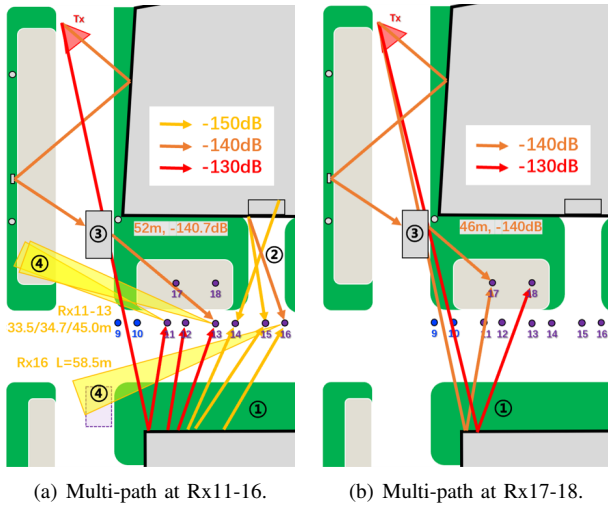


Fig. 6: Multi-path analysis at Rx11-18 (NLoS Rx points).

$$PL^{\alpha\beta} = 10 \times \alpha \times \log_{10} d + \beta + X_{\sigma_{SF}}^{\alpha\beta}, \quad (1b)$$

where PLE is the path loss exponent and d denotes the distance between Tx and Rx. The reference distance d_0 is equal to 1 m. The free-space path loss (FSPL) is given by the Friis' law. Moreover, α is the slope coefficient and β represents the optimized path loss offset in dB. $X_{\sigma_{SF}}^{CI}$ and $X_{\sigma_{SF}}^{\alpha\beta}$ are zero-mean Gaussian random variables with standard deviation σ_{SF}^{CI} and $\sigma_{SF}^{\alpha\beta}$ in dB, respectively, indicating the fluctuation caused by shadow fading.

The observations are drawn as follows. First, the omnidirectional PLEs are smaller since the power of all MPCs are added up, resulting in a lower omnidirectional path loss. Second, compared with the UMi-street canyon scenario specified in 3GPP TR 38.901, the omnidirectional PLE in the THz band is smaller in the LoS case but larger in the NLoS case. Third, compared to large-scale characteristics at 306-321 GHz, the path losses at 356-371 GHz are higher by 4-6 dB, and the shadow fading effect at 356-371 GHz is more

significant, as expected.

2) *Cluster parameters*: The numbers of clusters in the outdoor L-shaped street in the THz band are much smaller than that is specified in 3GPP UMi-street canyon scenario in frequency bands lower than 100 GHz. This fact indicates the strong sparsity in THz bands. To be specific, the average number of clusters at 300 GHz and 350 GHz is about 2-3 in LoS cases and 5-6 in NLoS cases. Furthermore, due to the sparsity of MPCs under the target 30 dB dynamic range, MPCs inside each cluster are more confined, and thus the intra-cluster delay and angular spreads are also much smaller.

3) *Delay and angular spreads*: We use the root-mean-square (RMS) delay spread (DS), azimuth spread of angle (ASA) and elevation spread of angle (ESA) to measure the power dispersion of MPCs in temporal and spatial domains [8]. First, the values of DS, ASA, and ESA in the NLoS case are noticeably larger than the counterparts in the LoS case. Second, in the LoS case, DS and ASA are normally smaller than 10 ns and 20° . For Rx points where the long vehicle-reflected ray is detected, the value of DS increases, which is still smaller than 20 ns at 306-321 GHz. Furthermore, the higher frequency band over 356-371 GHz has smaller DS and ASA. Besides, the values of spreads in the L-shaped street in the THz band are smaller than those in the UMi-street canyon scenario in 3GPP TR 38.901 in frequency bands lower than 100 GHz. Compared to results in the indoor L-shaped hallway¹, DS in the outdoor L-shaped street is smaller in the LoS case, while DS values in the NLoS case are comparable, in both frequency bands. ASAs are smaller in the outdoor L-shaped street for both cases and both frequency bands. Smaller power spreads in the outdoor L-shaped street in both temporal and spatial domains are attributed to the absence of walls that surround the scenario and thus confine MPCs with diverse delays and AoAs to the scenario.

¹The preliminary results in the indoor L-shaped hallway are presented in [8]. The measurement campaign is later extended to both 306-321 GHz and 356-371 GHz, and the complete characteristic analysis results are updated according to the same data processing procedure as this paper.

TABLE II: Summary of statistical channel parameters.

Scenario		L-shaped street 306-321 GHz		L-shaped street 356-371 GHz		3GPP 38.901 UMi-Street canyon 0.5-100 GHz				
Characteristic		LoS	NLoS	LoS	NLoS	LoS	NLoS			
Path loss (fitting)	CI	n_{best}	2.18	3.40	2.48	3.70	2.1	-		
		n_{omni}	1.94	3.07	2.19	3.36				
	$\alpha\beta$	α_{best}	2.84	11.12	3.20	16.86				
		β_{best}	73.73	-35.75	74.19	-117.88				
		α_{omni}	2.67	10.66	2.85	13.98				
		β_{omni}	72.84	-33.79	74.98	-78.96				
Shadow fading [dB]	CI	$\mu_{SF,best}$	0.13	0.06	0.14	0.10	-	-		
		$\sigma_{SF,best}$	1.94	6.83	2.72	8.56				
		$\mu_{SF,omni}$	0.14	0.06	0.13	0.08				
	$\alpha\beta$	$\sigma_{SF,omni}$	1.38	6.10	1.24	7.21				
		$\mu_{SF,best}$	0.00	0.00	0.00	0.00				
		$\sigma_{SF,best}$	1.61	6.20	2.44	7.03				
		$\mu_{SF,omni}$	0.00	0.00	0.00	0.00				
		$\sigma_{SF,omni}$	0.68	5.41	0.58	6.04				
		K-factor [dB]	μ_{KF}	6.84	8.20	8.25			8.26	9
			σ_{KF}	4.32	7.49	4.34			7.76	5
DS [\log_{10} s]	μ_{DS}	-8.42	-7.61	-8.78	-7.70	-7.7394	-7.4294			
	σ_{DS}	0.45	0.32	0.45	0.37	0.38	0.6796			
ASA [\log_{10} °]	μ_{ASA}	1.10	1.50	0.89	1.53	1.5302	1.6102			
	σ_{ASA}	0.31	0.35	0.55	0.36	0.3150	0.4249			
ESA [\log_{10} °]	μ_{ESA}	0.27	0.70	0.32	0.62	0.4802	0.8201			
	σ_{ESA}	0.18	0.11	0.23	0.16	0.2401	0.2352			
Cluster number		2.50	5.63	2.80	4.75	12	19			
Intra-cluster DS [ns]		0.37	1.83	0.23	0.30	5	11			
Intra-cluster ASA [°]		0.87	1.41	0.98	0.74	17	22			
Intra-cluster ESA [°]		1.17	1.83	1.14	1.18	7	7			

IV. CONCLUSION

In this paper, we conducted a wideband channel measurement campaign in an L-shaped street on the university campus at 306-321 GHz and 356-371 GHz. The scenario contains one street along the parking area, and another perpendicular street canyon between two buildings. The characteristics of multipath propagation are elaborated to identify major scatterers in the environment and their impact on MPCs. We analyze the outdoor THz channel characteristics in the two frequency bands, and draw the following observations.

- First, reflected and scattered rays on the wall are well observed. Forward-reflected rays endure extra loss about 5-15 dB, while back-reflected rays endure extra loss about 20-30 dB. Besides, the abundance of scattering on the wall is demonstrated by PDAP results.
- Second, other major scatterers, i.e., traffic signs, lamps, and vehicles, are identified in this outdoor scenario. For instance, the traffic sign and the lamp result in additional reflection losses about several decibels and 15 dB, respectively.
- Third, the interaction on the vehicle is investigated. While transmission or reflection renders an extra loss less than 10 dB, the scattering on vehicles are much less significant.
- Fourth, as the receiving point moves from LoS positions

into the street canyon (Street B) between two high buildings, the LoS is blocked by the building. For NLoS receiving points as far as 20 m away from the open crossroad, i.e., the entrance of the street canyon, the received power is 20 dB lower than that of the LoS point at the crossroad.

- Fifth, we further analyzed THz channel characteristics in the outdoor scenario, and compared our results with those in the UMi-street canyon scenario below 100 GHz, which indicates the sparsity of MPCs and smaller power spreads in both temporal and spatial domains in the THz band.

REFERENCES

- [1] I. F. Akyildiz, C. Han, Z. Hu, S. Nie, and J. M. Jornet, "Terahertz Band Communication: An Old Problem Revisited and Research Directions for the Next Decade," *IEEE Transactions on Communications*, vol. 70, no. 6, pp. 4250–4285, Jun. 2022.
- [2] Z. Chen, C. Han, Y. Wu, L. Li, C. Huang, Z. Zhang, G. Wang, and W. Tong, "Terahertz Wireless Communications for 2030 and Beyond: A Cutting-Edge Frontier," *IEEE Communications Magazine*, vol. 59, pp. 66–72, Nov. 2021.
- [3] T. S. Rappaport, Y. Xing, O. Kanhere, S. Ju, A. Madanayake, S. Mandal, A. Alkhateeb, and G. C. Trichopoulos, "Wireless Communications and Applications Above 100 GHz: Opportunities and Challenges for 6G and Beyond," *IEEE Access*, vol. 7, pp. 78 729–78 757, Jun. 2019.
- [4] C. Han, Y. Wang, Y. Li, Y. Chen, N. A. Abbasi, T. Kürner, and A. F. Molisch, "Terahertz Wireless Channels: A Holistic Survey on Measurement, Modeling, and Analysis," *IEEE Communications Surveys & Tutorials*, vol. 24, no. 3, pp. 1670–1707, Jun. 2022.
- [5] N. A. Abbasi, J. Gomez-Ponce, R. Kondaveti, S. M. Shaikbepari, S. Rao, S. Abu-Surra, G. Xu, C. Zhang, and A. F. Molisch, "THz Band Channel Measurements and Statistical Modeling for Urban D2D Environments," *IEEE Transactions on Wireless Communications (Early Access)*, Jun. 2022.
- [6] S. Ju, Y. Xing, O. Kanhere, and T. S. Rappaport, "Sub-Terahertz Channel Measurements and Characterization in a Factory Building," in *Proc. of IEEE ICC Workshops*, May 2022.
- [7] International Telecommunication Union - Radiocommunication Sector, "World Radiocommunication Conference 2019 (WRC-19) - Final Acts," ITU Publications, Geneva, Switzerland, Mar. 2020.
- [8] Y. Wang, Y. Li, Y. Chen, Z. Yu, and C. Han, "0.3 THz Channel Measurement and Analysis in an L-shaped Indoor Hallway," in *Proc. of IEEE ICC*, pp. 1–6, Jun. 2022.
- [9] Y. Li, Y. Wang, Y. Chen, Z. Yu, and C. Han, "Channel Measurement and Analysis in an Indoor Corridor Scenario at 300 GHz," in *Proc. of IEEE ICC*, pp. 1–6, Jun. 2022.
- [10] T. Doeker, J. M. Eckhardt, and T. Kürner, "Channel Measurements and Modeling for Low Terahertz Communications in an Aircraft Cabin," *IEEE Transactions on Antennas and Propagation*, Jul. 2022.
- [11] F. Undi, A. Schultze, W. Keusgen, M. Peter, and T. Eichler, "Angle-Resolved THz Channel Measurements at 300 GHz in an Outdoor Environment," in *Proc. of IEEE ICC Workshops*, pp. 1–7, Jun. 2021.
- [12] K. Guan, D. He, B. Ai, Y. Chen, C. Han, B. Peng, Z. Zhong, and T. Kürner, "Channel Characterization and Capacity Analysis for THz Communication Enabled Smart Rail Mobility," *IEEE Transactions on Vehicular Technology*, vol. 70, no. 5, pp. 4065–4080, Apr. 2021.
- [13] J. M. Eckhardt, V. Petrov, D. Moltchanov, Y. Koucheryavy, and T. Kürner, "Channel Measurements and Modeling for Low Terahertz Band Vehicular Communications," *IEEE Journal on Selected Areas in Communications*, vol. 39, no. 6, pp. 1590–1603, Apr. 2021.
- [14] 3GPP, "Study on channel model for frequencies from 0.5 to 100 GHz," 3rd Generation Partnership Project (3GPP), Technical Report (TR) 38.901, Dec. 2019, version 16.1.0.
- [15] Y. Li, Y. Wang, Y. Chen, Z. Yu, and C. Han, "Channel Measurement and Characterization with Modified SAGE Algorithm in an Indoor Corridor at 300 GHz," *arXiv preprint arXiv:2203.16745*, 2022.